

# Bolometric technique for high-resolution broadband microwave spectroscopy of ultra-low-loss samples

P. J. Turner, D. M. Broun,\* Saeid Kamal,\* M. E. Hayden,\* J. S. Bobowski,

R. Harris, D. C. Morgan, J. S. Preston,† D. A. Bonn, and W. N. Hardy

*Department of Physics and Astronomy, University of British Columbia, Vancouver, B.C., Canada V6T 1Z1*

(Dated: October 25, 2018)

A novel low temperature bolometric method has been devised and implemented for high-precision measurements of the microwave surface resistance of small single-crystal platelet samples having very low absorption, as a continuous function of frequency. The key to the success of this non-resonant method is the *in-situ* use of a normal metal reference sample that calibrates the absolute rf field strength. The sample temperature can be controlled independently of the 1.2 K liquid helium bath, allowing for measurements of the temperature evolution of the absorption. However, the instrument's sensitivity decreases at higher temperatures, placing a limit on the useful temperature range. Using this method, the minimum detectable power at 1.3 K is 1.5 pW, corresponding to a surface resistance sensitivity of  $\approx 1 \mu\Omega$  for a typical 1 mm $\times$ 1 mm platelet sample.

## I. INTRODUCTION

In this article we describe an apparatus designed for the continuous-frequency measurement of low temperature electromagnetic absorption spectra in the microwave range. The motivation to develop this instrument comes from a desire to resolve, in great detail, the microwave conductivity of high-quality single crystals of high- $T_c$  cuprate superconductors. However, the technique we describe should find a wealth of applications to other condensed matter systems, providing a means to explore the dynamics of novel electronic states with unprecedented resolution. The possibilities include: the physics of the metal-insulator transition, where charge localization should lead to frequency scaling of the conductivity; electron spin resonance spectroscopy of crystal field excitations; ferromagnetic resonance in novel magnetic structures; and cyclotron resonance studies of Fermi surface topology. In addition to the cuprate superconductors, other natural possibilities in the area of superconductivity include heavy fermion and ruthenate materials, as well as high resolution spectroscopy of low-frequency collective excitations such as Josephson plasmons and order-parameter collective modes.

Early microwave measurements on high quality single crystals of  $\text{YBa}_2\text{Cu}_3\text{O}_{7-\delta}$  showed that cooling through  $T_c \approx 90$  K decreased the surface resistance very rapidly, by four orders of magnitude at 2.95 GHz, reaching a low temperature value of several  $\mu\Omega$ .<sup>1</sup> Resolving this low absorption in the microwave region has provided a technical challenge that has been successfully met over most of the temperature range below  $T_c$  by the use of high precision cavity-perturbation techniques.<sup>2,3</sup> In these experiments, the sample under test is brought into the microwave fields of a high quality-factor resonant structure made from superconducting cavities or low-loss dielectric pucks. A limitation of such techniques is that the resonator is generally restricted to operation at a single fixed frequency, therefore requiring the use of many separate experiments in order to reveal a spectrum. Furthermore, a very gen-

eral limitation of the cavity perturbation method is that the dissipation of the unknown sample must exceed the dissipation of the cavity itself in order to be measured with high precision — a very strong demand for a high quality superconductor in the  $T \rightarrow 0$  limit. The measurement of the residual absorption in superconductors is challenging at any frequency: in the case of infra-red spectroscopy the problem becomes that of measuring values of reflectance that are very close to unity. The challenge lies in the calibration of the measurement, and in both microwave and infra-red work, one relies on having a reference sample of known absorption to calibrate the loss in the walls of the microwave resonator or the infra-red reflectance. Despite these limitations, resonant microwave techniques are the only methods with sufficient sensitivity to measure the evolution of the microwave absorption over a wide temperature range. In a recent effort by our group, five superconducting resonators were used to map a coarse conductivity spectrum from 1 GHz to 75 GHz in exceptionally clean samples of  $\text{YBa}_2\text{Cu}_3\text{O}_{6.99}$  from 4 K to 100 K.<sup>4</sup> This work revealed low temperature quasiparticle dynamics inconsistent with simple models of  $d$ -wave superconductivity, whose key signatures appear in the frequency dependence of the conductivity.<sup>5,6,7</sup> The failure of simple theories to give a complete description of the temperature evolution and shape of the conductivity spectra in the best quality samples has driven us to develop the technique described here, with the result that we can now resolve low-temperature microwave conductivity spectra in unprecedented detail.

Bolometric detection is a natural method for measuring the surface resistance spectrum over a continuous frequency range. For any conductor, the power absorption in a microwave magnetic field is directly proportional to the surface resistance  $R_s$ :

$$P_{abs} = R_s \int H_{r,f}^2 dS, \quad (1)$$

where  $H_{r,f}$  is the r.m.s. magnitude of the tangential magnetic field at the surface  $S$ . As a result, a measurement of

the temperature rise experienced by a weakly-thermally-anchored sample exposed to a known microwave magnetic field  $H_{rf}$  directly gives  $R_s$ . To enhance rejection of spurious temperature variations, the rf power should be amplitude modulated at low frequency and the resulting temperature oscillations of the sample detected synchronously.

We note that as part of a pioneering study of superconducting Al, a similar bolometric microwave technique was used by Biondi and Garfunkel to examine the detailed temperature dependence of the superconducting gap frequency.<sup>8</sup> This earlier experiment had the simplifying advantage of measuring the absorption by a large waveguide made entirely from single crystalline Al. Unfortunately, in more complicated materials such as the multi-elemental cuprate superconductors, the best quality samples can only be produced as small single crystals. More recently, frequency-scanned bolometric measurements have proven useful in probing collective excitations in small samples of high- $T_c$  cuprates at frequencies above 20 GHz where the absorption is larger and much easier to measure.<sup>9</sup> These techniques, however, have not focussed on the challenge of resolving the low temperature absorption of high-quality single crystals across a broad frequency range.

A characteristic feature of many electronic materials of current interest is reduced dimensionality, which gives rise to highly anisotropic transport coefficients. When making microwave measurements, a well-defined geometry must be chosen in order to separate the individual components of the conductivity tensor, and also to ensure that demagnetization effects do not obscure the measurement. One particularly clean approach that has been widely used places the sample to be characterized near a position of high symmetry in a microwave enclosure, in the quasi-homogeneous microwave magnetic field near an electric node. Often, single crystal samples grow naturally as platelets having a broad  $\hat{a}$ - $\hat{b}$  plane crystal face and thin  $\hat{c}$ -axis dimension, and demagnetization effects are minimized if the broad face of the sample is aligned parallel to the field. In response to the applied rf magnetic field, screening currents flow near the surface of the sample along the broad  $\hat{a}$  or  $\hat{b}$  face and must necessarily flow along the  $\hat{c}$  direction to complete a closed path. In some cases, it is desirable to work with samples that are very thin, rendering the  $\hat{c}$ -axis contribution negligible. Alternatively, by varying the aspect ratio of the sample by either cleaving or polishing, one can make a series of measurements to disentangle the different crystallographic contributions, without having to change samples. For example, in the cuprate superconductors, the conductivity parallel to the two dimensional  $\text{CuO}_2$  plane layers can be several orders of magnitude larger than that perpendicular to the weakly-coupled planes. Typical as-grown crystal dimensions are  $1.0 \times 1.0 \times .01 \text{ mm}^3$ . For this aspect ratio, experiments where a sample was cleaved into many pieces showed that the  $\hat{c}$ -axis contribution is unimportant.<sup>10</sup> We note here that all measurements

presented in this article employ the low-demagnetization sample orientation discussed above.

The broadband surface-resistance measurement technique we describe in the following sections provides three distinct technical advances over previous bolometric approaches: a uniform microwave field configuration in the sample region that permits the separation of anisotropic conductivity components; the use of an *in-situ* reference sample that calibrates the microwave field strength at the sample absolutely; and very high sensitivity afforded by the choice of a resistive bolometer optimized for the low-temperature range and mounted on a miniaturized thermal stage. These features of our apparatus permit precision measurements of the absolute value of  $R_s(\omega, T)$  in very-low-loss samples down to 1.2 K and over the frequency range 0.1-21 GHz. We will briefly demonstrate that this range captures the key frequency window for long-lived nodal quasiparticles in extremely clean samples of  $\text{YBa}_2\text{Cu}_3\text{O}_{7-\delta}$ , and to further demonstrate the performance and versatility of the apparatus, we also show an example of zero-field electron-spin-resonance spectroscopy.

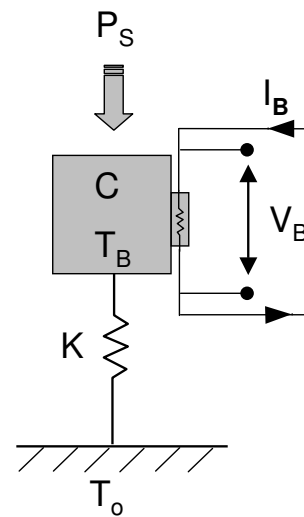


FIG. 1: A simple thermal model consisting of a heat capacity  $C$  thermally isolated from base temperature  $T_0$  by a weak thermal link of conductance  $K$ . The resistive bolometer is thermally anchored to  $C$  and monitors its temperature,  $T_B$ , which is elevated above  $T_0$  by a constant current bias  $I_B$  passing through the bolometer. The absorption of incident signal power  $P_s$  causes heating in  $C$ , detectable as a temperature rise through a change in the voltage  $V_B$ .

## II. BOLOMETRIC DETECTION

It is instructive to calculate the minimum power detectable by a simple thermal stage, the temperature of which is monitored by a resistive bolometer, as depicted in Fig. 1.<sup>11</sup> The bolometer has a resistance  $R_B$  and is in thermal equilibrium with a larger heat capac-

ity  $C$  representing contributions from the sample, its holder, and the weak thermal link. This combination is weakly connected, via a thermal conductance  $K$ , to a heat sink maintained at base temperature  $T_0$ . The bolometer is heated to its operating temperature  $T_B$  by a bias power  $P_B = I_B^2 R_B$ , where  $I_B$  is the fixed bolometer bias current. For this analysis we do not consider feedback effects, although they are very important in the special case of transition edge bolometers.<sup>12</sup> As a result, we consider a configuration where  $I_B$  provides only modest self-heating of the bolometer, such that  $\gamma \equiv (T_B - T_0)/T_0 \lesssim 1$ . An incident signal power  $P_S$  raises the temperature by an amount  $\delta T_B = P_S/K$ , causing a change in the readout voltage across the bolometer  $\delta V_B = I_B(dR_B/dT)\delta T_B = I_B(dR_B/dT)P_S/K$ . We then define a threshold detectable signal level that is equal to the thermal noise  $v_n$  generated in a bandwidth  $\Delta\nu$  in the bolometer,  $\overline{v_n^2} = 4k_B T_B R_B \Delta\nu$ . It is then possible to write an expression for the minimum detectable power  $P_S^{min}$  in terms of the dimensionless sensitivity of the bolometer  $S_d = T/R|dR/dT|$ , typically of the order of unity, the noise power  $P_n = k_B T_B \Delta\nu$ , and the bolometer bias power  $P_B$ :

$$P_S^{min} = \frac{2}{\gamma S_d} \sqrt{P_n P_B}. \quad (2)$$

From this expression one immediately sees that it is desirable to minimize both the bias and noise powers, within the combined constraints of maintaining the bolometer temperature at  $T_B$  and keeping the thermal response time fixed at a suitably short value. By miniaturization of the sample holder, the bias power required to reach a given temperature can be considerably reduced, while at the same time maintaining a practical thermal time constant. The noise power is limited intrinsically by the thermal (Johnson) noise from the bolometer resistance at temperature  $T_B$ . However, most real sensors show substantial excess noise, and the Cernox 1050 sensor<sup>14</sup> used in the present implementation of our experiment is no exception, showing approximately 40 dB of excess noise in the presence of a 1.3  $\mu\text{A}$  bias current. This completely accounts for the discrepancy between the minimum detectable power at 1.3 K of 17 fW calculated using Eq. 2 assuming only Johnson noise, and the experimentally determined value of 1.5 pW.

### III. BROADBAND ABSORPTION MEASUREMENT APPARATUS

For our method of bolometric detection to be most useful, it is necessary to deliver microwaves to the sample across a broad range of frequency and, at the same time, not only accurately control the polarization of the microwave field at the sample, but also maintain a fixed relationship between the field intensity at the sample under test and the field intensity at the reference sample. Essential to this is the design of the microwave wave-

guide. We use a custom-made transmission line, shown in cross-section in Fig. 2, that consists of a rectangular outer conductor that measures 8.90 mm  $\times$  4.06 mm in cross-section and a broad, flat centre conductor, or septum, that measures 4.95 mm  $\times$  0.91 mm. This supports a TEM mode in which the magnetic fields lie in the transverse plane and form closed loops around the centre conductor, setting a fixed relationship between the microwave field strengths on either side of the septum. The line is terminated by shorting the centre conductor and outer conductor with a flat, metallic endwall. This enforces an electric field node at the end of the waveguide, adjacent to which we locate the small platelet sample and reference, with their flat faces parallel and very close to the endwall. The broad centre conductor ensures spatially uniform fields over the dimensions of the sample, making it possible to drive screening currents selectively along a chosen crystallographic direction. The electro-dynamics of the rectangular waveguide are discussed in more detail in Appendix B. A strong variation in the power delivered to the sample as a function of frequency arises due to standing waves in the microwave circuit. In order to properly account for this, we have incorporated an *in-situ* normal-metal reference sample of known surface resistance that acts as an absolute power meter. This second sample is held in a position that is electromagnetically equivalent to the that of the test sample, on a separate thermal stage.

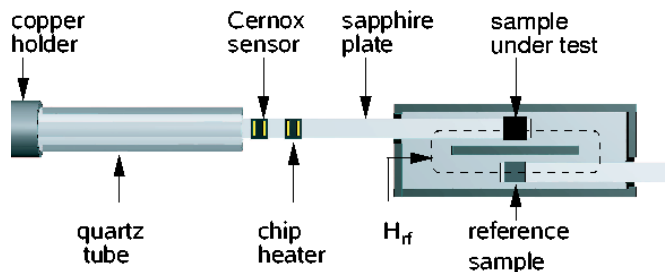


FIG. 2: Schematic cross-section of the terminated coaxial line region showing the sample and reference materials suspended on sapphire plates in symmetric locations in the rf magnetic field. The sapphire plate is epoxied into the bore of a quartz tube which thermally isolates it from the copper holder, fixed at the temperature of the 1.2 K helium bath.

One of the challenges of cryogenic microwave absorption measurements on small, low-loss samples is the design of the sample holder, which must measure and regulate the sample temperature, and yet contribute negligible dissipation compared to the sample. A widely used technique that satisfies these requirements is that of a sapphire hot-finger in vacuum,<sup>13</sup> allowing the thermometry to be electromagnetically shielded from the microwave fields. In our apparatus, the sample holder is inserted through a hole that is beyond cut off for all operating frequencies. For ac calorimetric measurements, the design of the thermal stage is critical in setting the sensitivity of the system. The experimental arrangement

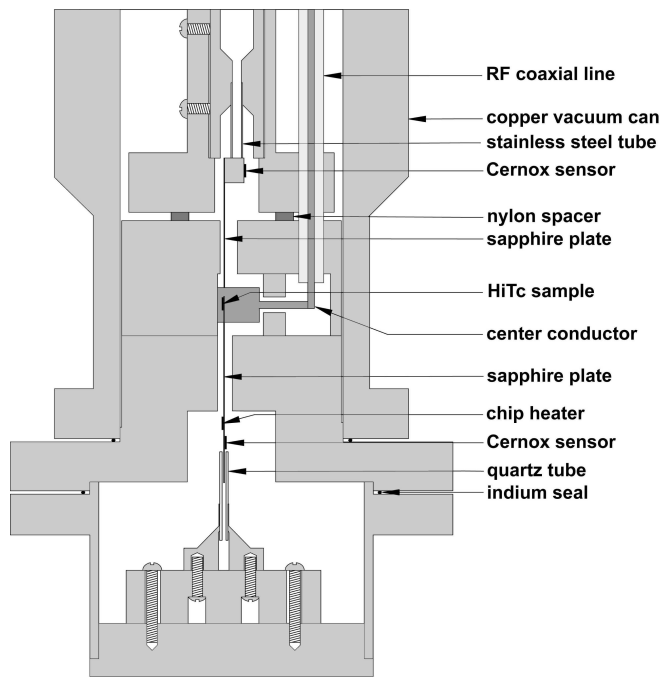


FIG. 3: Scale drawing of the assembled apparatus indicating the details of the vacuum can and sample region. The alloy reference sample is not visible in this cut-away view.

is shown schematically in Fig. 2 with the sample under test fixed on the end of a  $100\ \mu\text{m}$  thick sapphire plate using a tiny amount of vacuum grease.<sup>15</sup> The plate extends 17 mm from the sample to where it is epoxied into the bore of a 1.2 mm diameter quartz glass tube that acts as a thermal weak-link to the liquid helium bath. A Cernox thermometer and a  $1500\ \Omega$  surface-mount resistor used as a heater<sup>16</sup> are glued directly onto the sapphire plate with a very thin layer of Stycast 1266 epoxy,<sup>17</sup> ensuring intimate thermal contact with the sapphire and hence the sample. We use 0.05 mm diameter NbTi superconducting electrical leads to the thermometer and heater for their very low thermal conductance, which is in parallel with the quartz weak-link.

The microwave circuit is powered by a Hewlett-Packard 83630A synthesized sweeper (0.01-26.5 GHz) combined with either an 8347A (0.01-3 GHz) or 8349B (2-20 GHz) amplifier, generating up to 23 dBm of rf power across the spectrum. Approximately 2 m of 0.141" stainless steel coaxial line<sup>18</sup> delivers power from the amplifier down the cryostat to the vacuum can where it is soldered into the rectangular line (see Fig. 3). The r.m.s. microwave magnetic field amplitude at the samples is typically  $\sim 10^{-2}$  Oersteds, which generates  $\sim \mu\text{K}$  modulations in the sample-stage temperature for a typical high quality  $1\ \text{mm}^2$  high- $T_c$  sample having a low frequency  $R_s$  value of  $1\ \mu\Omega$ .

An assembled view of the low temperature apparatus including the microwave transmission line and the positions of the sample and reference holders is provided in

Fig. 3. The sapphire plates that support both the test sample and reference sample are inserted through 4 mm cut-off holes into the microwave magnetic field. The rectangular coaxial line consists of a centre conductor made from a 0.91 mm thick copper plate soldered at one end onto the centre conductor of the 0.141" semi-rigid coaxial line, and at the other end into the wall of the copper cavity that comprises the outer conductor of the transmission line. To minimize the rf power dissipated in the low temperature section of transmission line, the entire surface exposed to microwave radiation, including the final 15 cm of semi-rigid coaxial line, was coated with PbSn solder, which is superconducting below 7 K. During experiments, the vacuum can is completely immersed in a pumped liquid helium bath having a base temperature of 1.2 K.

The selection of a reference material for low-frequency work must be made carefully. Initially, we chose samples cut from commercially available stainless-steel shim stock, a common choice in infrared spectroscopy work. Calibration experiments produced erratic results which were eventually traced to the presence of anisotropic residual magnetism in the stainless steel. Subsequently, we produced our own reference material, choosing an Ag:Au alloy (70:30 at.% made from 99.99% pure starting materials), because it exhibits a very simple phase diagram that guarantees homogeneity.<sup>19</sup> By using an alloy, we ensure that the electrostatics remain local at microwave frequencies, avoiding the potential complications arising from the anomalous skin effect.<sup>20</sup> Our sample was cut from a  $93 \pm 5\ \mu\text{m}$  thick foil having a measured residual dc resistivity value of  $\rho = 5.28 \pm 0.3\ \mu\Omega\text{cm}$ , constant below 20 K.

While the thermal stage for the reference sample is similar in design to that used for the sample under test, it uses a higher conductance stainless steel thermal weak-link (in place of the quartz tube), since the dissipation of the normal metal calibration sample is orders of magnitude larger than that of a typical superconducting sample. Because the apparatus was implemented as a retrofit to an existing experiment, the reference thermal stage had to be mounted directly onto the body of the transmission line structure. Although the cavity walls are superconducting to reduce their absorption, we use a nylon spacer to thermally isolate the base of the reference from the transmission line to avoid direct heating. The heat-sinking of the reference base to the helium bath is made using a separate copper braid that is not visible in Fig. 3.

As considered previously in our generic analysis, we operate the Cernox bolometer with a constant dc current bias, typically a few  $\mu\text{A}$ , provided by the series combination of an alkaline battery (1.5 V or 9 V) and bias resistor whose value is much larger than that of the Cernox sensor. With the helium bath under temperature regulation, the choice of bias power sets the temperature of the sample for a given experiment, with no other temperature control necessary. All electrical leads into the cryostat are shielded twisted pairs of insulated man-

ganin wire, and true four-point resistance measurements are made on all sensors. The voltage signal appearing on the Cernox thermometer is amplified outside the cryostat by a carefully shielded and battery-powered circuit. We use a two-stage cascaded amplifier with one Analog Devices AD548 operational amplifier per stage, chosen because these are readily available, low-noise amplifiers. The dc level is nulled between stages to prevent saturation, and the total gain is  $10^4$ . The amplified signal, corresponding to the temperature modulation of the sample, is then demodulated with a Stanford Research Systems SR850 digital lock-in amplifier that is phase-locked with the rf-power amplitude modulation. There are two such systems, one for the sample and one for the reference measurements. The entire experiment is operated under computer control when collecting data.

#### IV. CALIBRATION

Two steps are necessary for an absolute calibration of the surface resistance of an unknown specimen from the measured temperature-rise data. The first is to calibrate the absolute power sensitivity of the sample and reference thermal stages at the actual operating temperature and modulation frequency. This is achieved using the small *in-situ* heater to drive well-characterized heat pulses that mimic absorption by the sample, while at the same time measuring the corresponding temperature response. The second step requires the calibration of the magnetic field strength at the sample, at each frequency, using the known absorption of the reference sample. We exploit the fact that the metallic reference sample experiences the same incident microwave field  $H_{rf}$  as the sample under test, guaranteed by conservation of magnetic flux. This ensures that taking the ratio of the absorbed power per unit surface area of each sample provides the ratio of the surface resistance values:

$$\frac{P_{abs}^{sam}}{P_{abs}^{ref}} = \frac{R_s^{sam} A^{sam}}{R_s^{ref} A^{ref}}. \quad (3)$$

The surface resistance of the unknown sample  $R_s^{sam}(\omega)$  is then trivially found by multiplying the power-absorption ratio, shown in Fig. 4, by  $R_s(\omega)$  of the metallic reference sample calculated using the classical skin-effect formula  $R_s(\omega) = \sqrt{\omega\mu_o\rho}/2$  where  $\omega/2\pi$  is the frequency and  $\mu_o$  is the permeability of free space. The raw power-absorption spectra, shown in the first two panels of Fig. 4, highlight the necessity of the reference sample. The absorption spectra of the samples is completely masked by the large amplitude variations of  $H_{rf}$  caused by the standing waves in the microwave circuit.

An essential test of the method is to make a frequency-scanned measurement with identical samples mounted on the sample and the reference stages. The result should be a frequency-independent ratio across the spectrum, equal to unity for samples with the same surface area.

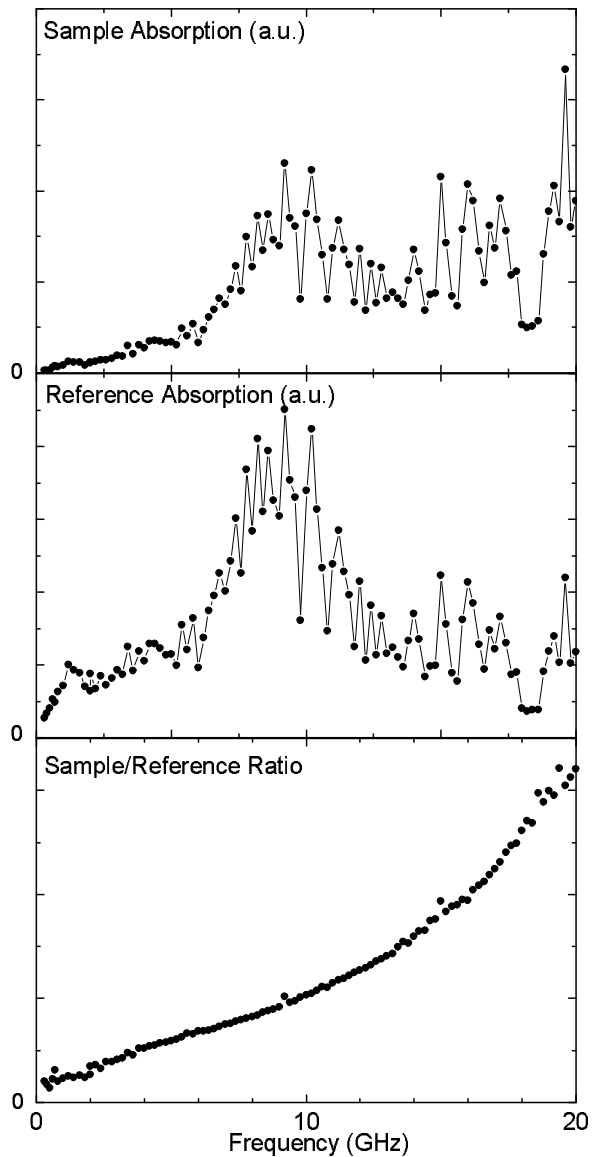


FIG. 4: Raw absorption spectra corresponding to the temperature rise of the sample. Taking the ratio of the two signals accounts for the strong frequency dependence of  $H_{rf}$  introduced by standing waves in the transmission line. The remaining frequency dependence of the ratio is due to the different  $R_s(\omega)$  spectra of the two samples.

In Fig. 5 we show such a measurement using two thin-platelet samples of our Ag:Au reference alloy, both at the base temperature of 1.2 K. The data reveal a ratio of 0.82 in the cryogenic apparatus, due to the fact that the centre conductor is offset from centre by 0.1 mm in the termination region, intensifying the fields on one side relative to the other. This scale factor must be included in the calibration of all experimental data. The sharp resonance seen in the ratio at 22.5 GHz indicates the presence of a non-TEM electromagnetic mode in the sample cavity that breaks the symmetry in field strength between sample and reference positions. For our present design,

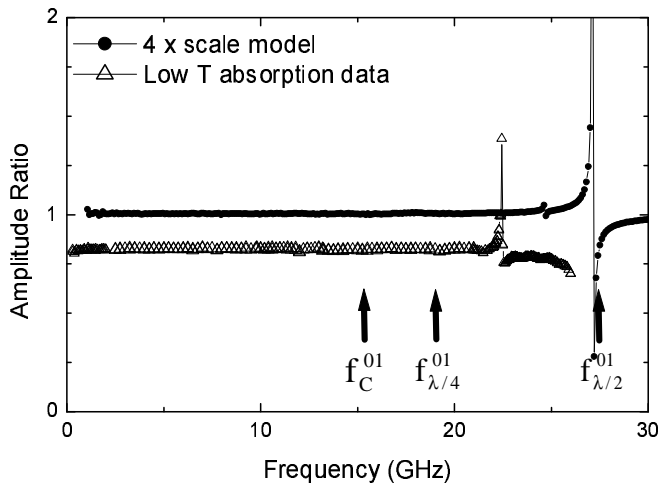


FIG. 5: Ratio of the sample absorption to reference absorption for identical samples, compared to measurements of the field amplitude at equivalent positions in a  $4\times$  scale model. (Frequencies for the scale model have been scaled by a factor of 4 for the comparison.) The ratio technique is seen to break down with a sharp resonance in both cases. The origin of these resonances, which limit the useful frequency range of the apparatus, is discussed in detail in Appendix B and shown to be due to the presence of standing waves of the  $TE_{01}$  waveguide mode. For this mode, the three arrows indicate: the cut-off frequency  $f_C^{01} = 15.38$  GHz at which the mode is first free to propagate; its quarter-wave resonance frequency  $f_{\lambda/4}^{01} = 19.11$  GHz, for open-circuit termination conditions; and the half-wave resonance frequency  $f_{\lambda/2}^{01} = 27.4$  GHz, for short-circuit termination conditions. The  $\lambda/4$  and  $\lambda/2$  resonance frequencies bracket the observed resonances. The scale model, which has a large transition capacitance between circular and rectangular coax sections, is seen to fall at the high end of the range.

this sets the upper frequency limit of operation.

In an attempt to gain further insight into the field configurations in the transmission line, and to understand how the higher order waveguide modes limit the upper frequency range, we built a scale model of the setup having all dimensions larger than those of the cryogenic apparatus by a factor of four. For comparison, a frequency scan of the model structure is included in Fig. 5, using loop-probes in the positions of the samples. The data show that the non-TEM-mode resonance occurs at 27 GHz, considerably higher than in the low temperature experiment. It turns out that the breakdown of the sample-reference symmetry occurs not at the frequency at which higher order waveguide modes first propagate in our structure, but at the frequency at which they form a resonant standing wave. A full discussion of this is given in Appendix B.

A number of other experimental tests were important to verify the proper operation of the system. Frequency scans without samples mounted on the sapphire stages confirmed that background absorption due to the sapphire and tiny amount of vacuum grease used to affix

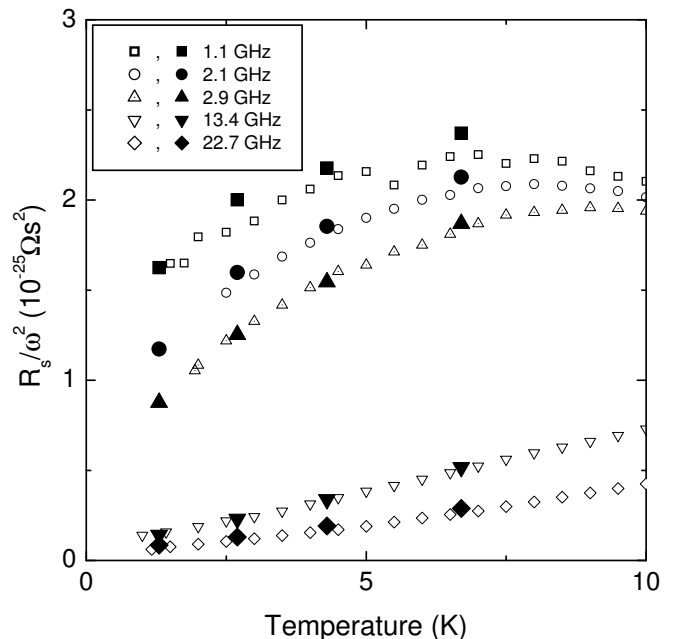


FIG. 6: Comparison of measurements made on the same sample of  $YBa_2Cu_3O_{6.50}$  using the broadband bolometric experiment (solid symbols) with those from five microwave resonators (open symbols). The agreement between methods is excellent. The data is plotted as  $R_s(\omega)/\omega^2$  to remove the frequency dependence associated with superfluid screening.

the samples is negligible — it is unmeasurable at low frequency, and contributes no more than  $2 \mu\Omega$  to an  $R_s$  measurement at 21 GHz. Scans without a sample also confirmed that no significant leakage heat current propagates to the thermometers directly from the microwave waveguide. The high thermal stability of the cryostat system is due in part to the very large effective heat capacity of the pumped 4 litre liquid-helium bath at 1.2 K. In addition, it is always important to make certain the temperature modulations of the samples are sufficiently small that the response of the thermal stages remains in the linear regime. Furthermore, measurements with the same sample located in different positions along the sapphire plate, with up to 0.5 mm displacement from the central location in the waveguide, confirmed that there is enough field homogeneity that our sample alignment procedure using an optical microscope is sufficient, and that samples of different sizes experience the same fields.

A very convincing verification of the technique is provided by the ability to compare broadband  $R_s(\omega, T)$  data with measurements of the *same sample* in five different high-Q microwave resonators. These experiments probe the temperature dependence of the absorption to high precision at a fixed microwave frequency: however, the determination of the *absolute* value of  $R_s$  is limited to about 10% as discussed previously. The bolometric method has the advantage of being able to measure a true spectrum because the dominant uncertainty, the absolute surface resistance of the reference sample, enters

as a scale factor that applies across the entire frequency and temperature range. A detailed discussion of the uncertainties in the bolometry data will be presented in the subsequent section. Figure 6 shows that there is very good agreement of both the temperature and frequency dependence of the surface resistance as measured independently by the fixed-frequency and broadband experiments.

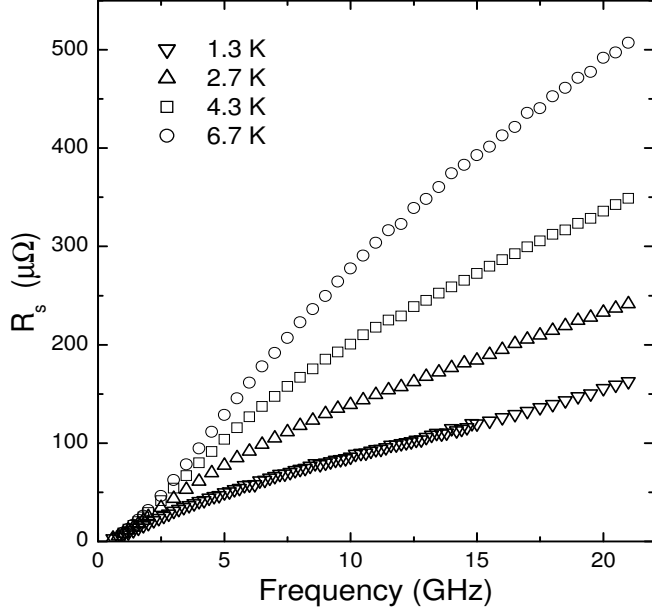


FIG. 7: Broadband measurements of the microwave surface resistance spectrum of  $\text{YBa}_2\text{Cu}_3\text{O}_{6.50}$  obtained with the bolometric apparatus below 10 K. The low frequency absorption approaches the resolution limit of the apparatus, while the upper frequency limit is imposed by the resonance in the microwave structure.

## V. PERFORMANCE

Figure 7 presents an example of high resolution broadband measurements of the frequency-dependent and temperature-dependent surface resistance of a superconducting sample.<sup>21</sup> This particular data set is for  $\hat{a}$ -axis currents in a  $\text{YBa}_2\text{Cu}_3\text{O}_{6.50}$  single crystal ( $T_c=56$  K) having dimensions  $1.25 \times 0.96 \times 0.010$  mm<sup>3</sup>. The data span the range 0.6-21 GHz, limited at high frequency by the resonance in the system, and at low frequency by the small dissipation of the sample, which approaches the resolution limit of the experiment. At 1 GHz, the values for the statistical r.m.s. uncertainty in surface resistance,  $\delta R_s$ , are about 0.2, 0.4, 0.6, and 1.3  $\mu\Omega$  for  $T = 1.3, 2.7, 4.3,$  and 6.7 K respectively. Error bars have been omitted from the figure for clarity. Systematic contributions to the uncertainty enter as overall scale factors in the  $R_s$  data and are attributed to an uncertainty in the DC resistivity of the thin Ag:Au alloy foil used as a reference

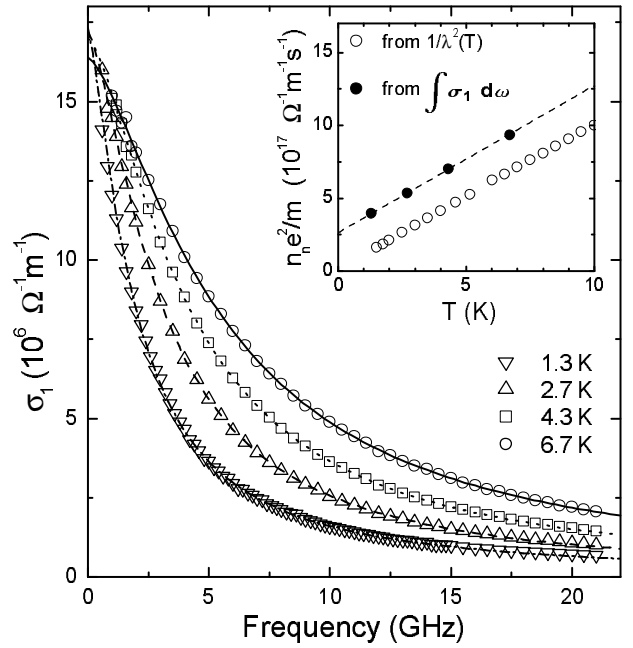


FIG. 8: The real part of the microwave conductivity  $\sigma_1(\omega, T)$  extracted from the broadband  $R_s(\omega, T)$  measurements. We use the self-consistent fitting procedure described in Appendix C to properly account for contributions to field-screening by the quasiparticles.

sample ( $\sim 5\%$ ), the surface area of the samples ( $\sim 1\%$ ), and the absolute power sensitivity of the thermal stage ( $\sim 1\%$ ).

The frequency dependence observed in  $R_s(\omega)$  is due to absorption by quasiparticles thermally excited from the superfluid condensate. The quantity of fundamental theoretical interest is the real part of the conductivity spectrum  $\sigma_1(\omega)$ , which must be extracted from the experimentally measured  $R_s(\omega)$  data. A thorough discussion of the method we use to do this is given in Appendix C but, to first approximation, the shape of the conductivity spectrum can be found by dividing  $R_s(\omega)$  by a factor of  $\omega^2$  to account for the screening of the applied field by the superfluid. Figure 8 shows the conductivity spectra extracted from the  $R_s(\omega)$  data using the complete analysis. It is immediately apparent why improving the sensitivity of the experiment is of the utmost importance. The low frequency region, where the power absorption becomes very small, is where the conductivity exhibits the strongest frequency dependence and is most important to measure accurately. The spectrum at 1.3 K has a width of the order of 5 GHz, signifying very long quasiparticle scattering times, indicative of the high quality of our  $\text{YBa}_2\text{Cu}_3\text{O}_{6.50}$  crystal. For this very clean sample, most of the spectral weight resides below the experimental frequency limit of 21 GHz at 1.3 K, but the increase in scattering with increasing temperature quickly broadens the spectra thus motivating future designs capable of probing a broader frequency range. Many cuprate ma-

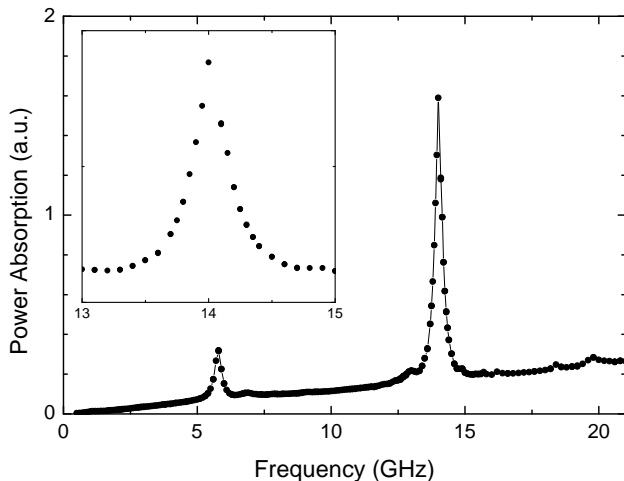


FIG. 9: The electromagnetic absorption spectrum of a  $Y_{0.99}Gd_{0.01}Ba_2Cu_3O_{6.99}$  single crystal at 1.3 K. The spectrum consists of a broad background due to the quasiparticle absorption in the superconductor in addition to the zero field ESR lines generated by the low concentration of magnetic  $Gd^{3+}$  impurities. Only ions residing within a distance  $\lambda$  of the crystal surface contribute to the signal as the applied rf field is strongly screened by the superconductor.

materials, such as  $Bi_2Sr_2CaCu_2O_{8+\delta}$ , have scattering rates that are orders of magnitude higher and require THz frequency techniques to probe their dynamics.<sup>22</sup>

As a final demonstration of the sensitivity of the broadband instrument we have described, we include a frequency scan of a superconducting sample that exhibits clearly discernable absorption lines due to zero field electron spin resonance (ESR) of a low density of magnetic impurities. Gadolinium ions (electron spin  $S = 7/2$ ) substitute for yttrium, sandwiched between the two CuO planes in the YBaCuO unit cell, and the splitting of the degenerate  $Gd^{3+}$  hyperfine levels by the crystalline field provides a very sensitive probe of the local microscopic structure.<sup>23</sup> These measurements are typically performed in a high field spectrometer, but the bolometric system provides a means of performing zero-field measurements. Figure 9 shows the 1.3 K absorption spectrum of a  $1\text{ mm}^2$   $Y_{0.99}Gd_{0.01}Ba_2Cu_3O_{6.99}$  single crystal consisting of a broad background due to the quasiparticle conductivity, essentially unaltered by the presence of the Gd ions, with the ESR absorption peaks superposed. The high signal-to-noise ratio achieved with the experiment allows one to resolve the spectrum in great detail.

The apparatus described here has sufficient sensitivity and frequency range for it to be immediately applicable to many other interesting problems in condensed matter physics. These might include: the study of low-lying collective modes in metals and superconductors; zero-field electron spin resonance in correlated insulators; and the study of critical phenomena at the metal-insulator transition and near the zero-temperature magnetic critical

points that occur in certain  $d$ - and  $f$ -electron metals. With a little attention to thermal design, specifically the thermal separation of sample stages from the microwave waveguide, the superconducting coatings on the waveguide could be removed and the system used in high magnetic fields. This would open interesting possibilities in the area of metals physics, such as high-resolution cyclotron and periodic-orbit resonance, as well as the study of vortex dynamics and vortex-core spectroscopy in superconductors. Finally, further miniaturization of the experiment should also be possible: the ultimate goal would be to extend the frequency range of this type of spectroscopy so that it joins seamlessly on to the THz range now accessible using pulsed-laser techniques.

### Acknowledgments

The authors are indebted to Pinder Dosanjh for his technical assistance, as well as to Ruixing Liang for the YBaCuO samples employed in these experiments. We also acknowledge financial support from the Natural Science and Engineering Research Council of Canada and the Canadian Institute for Advanced Research.

### APPENDIX A: FREQUENCY RESPONSE OF DISTRIBUTED THERMAL STAGE

We wish to calculate the temperature response of a simple thermal stage to a sinusoidal heat flux  $P_{in} = \text{Re}\{\tilde{P}_0 e^{i\omega t}\}$  superimposed on a static temperature gradient. We consider an arrangement where the isothermal sample stage has negligible thermal mass and is connected to base temperature by a weak thermal link with distributed heat capacity  $c_V$  per unit volume. It is a straightforward extension to include an additional lumped heat capacity for the isothermal stage; once the lumped heat capacity dominates, the frequency response simplifies to that of a single-pole low-pass filter. However, in our case this is unnecessary: for electrodynamic measurements at low temperatures, the sample holder is required to be both electrically insulating and highly crystalline, and will therefore have very low heat capacity.

Here we consider the one-dimensional problem of a thin bar (the quartz tube in our apparatus) of length  $\ell$  and cross-sectional area  $A$ , with one end fixed at a base temperature  $T_0$  while the other end is heated by a heat flux due to sample power absorption. The propagation of a heat current  $J_Q$  through the bar is constrained by the continuity equation  $\partial J_Q / \partial x + c_V \partial T / \partial t = 0$  and the thermal conductivity  $\kappa$  is defined by  $J_Q = -\kappa \partial T / \partial x$ . Together, these lead to the one-dimensional heat equation  $\partial T / \partial t = \alpha \partial^2 T / \partial x^2$  where  $\alpha = \kappa / c_V$  is the thermal diffusivity. Defining a complex thermal diffusion length  $\tilde{\delta} = \sqrt{\alpha / i\omega}$ , the time-dependent part of the temperature



profile can be written

$$\Delta T(x, t) = \text{Re} \left\{ \tilde{T} e^{i\omega t} \sinh(x/\tilde{\delta}) \right\} \quad (\text{A1})$$

where  $\tilde{T}$  is fixed by the heat-flux boundary condition:  $P_{in} = -\kappa A (\partial T / \partial x)|_{x=\ell}$ . This completely determines the frequency-dependent temperature rise of the sample stage:

$$\Delta T(\ell, t) = \text{Re} \left\{ \frac{\tilde{P}_0}{\kappa A} \tilde{\delta} e^{i\omega t} \tanh(\ell/\tilde{\delta}) \right\} \quad (\text{A2})$$

In the low frequency limit, the temperature rise reverts to the usual result:

$$\Delta T(\ell, t) = \frac{P_0 \ell}{\kappa A} \cos(\omega t), \quad (\text{A3})$$

where, without loss of generality, we have set the phase of the input heat flux to zero. In the high frequency limit, the thermal diffusion length becomes shorter than the weak link and the temperature rise is reduced, being given by:

$$\Delta T(\ell, t) = \frac{P_0 |\tilde{\delta}|}{\kappa A} \cos(\omega t - \pi/4) \quad (\text{A4})$$

where  $|\tilde{\delta}| = \sqrt{\alpha/\omega}$ . At finite frequencies, part of the heat flux is diverted into the distributed heat capacity of the thermal link. For a fixed input power (and hence fixed temperature *gradient* at the end of the thermal link) this leads to smaller temperature rises and a decreased sensitivity of the bolometric method. Clearly, the experimental sensitivity of the bolometric method will be optimized by operating in the low-frequency limit:  $|\tilde{\delta}| > \ell$  or  $\omega < \alpha/\ell^2$ . A consideration of the thermal diffusivity and dimensions of the weak-link must therefore be part of any plan to increase the modulation frequency.

Fig. 10 shows the frequency response of the sample thermal stage in our apparatus when it was subjected to a sinusoidally varying heater power, normalized to the static response. Included in the figure are fits to the distributed-heat-capacity model, Eq. A2 and a single-pole low-pass filter response  $\Delta T(\omega)/\Delta T(\omega=0) = 1/\sqrt{1 + \omega^2 \tau^2}$ . Although both curves fit the data well over most of the frequency range, the best-fit value of the time constant  $\tau$  in the lumped-element model corresponds to a heat capacity much larger than the calculated heat capacity of the sapphire sample stage. Instead, the value obtained from the fit is approximately half the heat capacity of the quartz tube, indicating the correct physics is that of heat diffusion in a distributed thermal system.

## APPENDIX B: DESIGN STRATEGY FOR RECTANGULAR COAXIAL TRANSMISSION LINE

In optimizing a microwave transmission line for the bolometric measurement of surface resistance the guid-

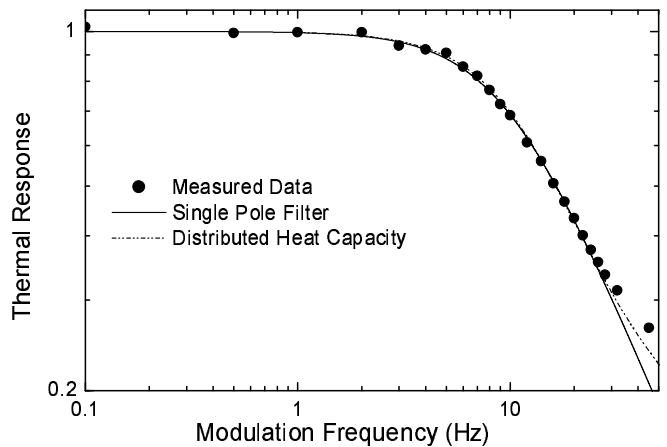


FIG. 10: Low temperature ( $T = 1.3$  K) measurements of the dynamic thermal response of the quartz-tube bolometer platform. Curves on the plot show fits using lumped and distributed heat capacity models.

ing aims must be: to deliver microwave power efficiently to the sample region, over as wide a frequency range as possible and with a well defined polarization; to have regions of uniform microwave magnetic field at the sample and reference positions; and, at these positions, to have a fixed, frequency-independent ratio between the field strengths. These aims can be met by using an impedance-matched ( $50 \Omega$ ), single-mode coaxial line, with rectangular cross section and a broad, flat center conductor or septum, as shown in Fig. 11(i). In addition, the dimensions of the rectangular coaxial line should be chosen carefully, to prevent higher-order waveguide modes from entering the operating frequency range of the experiment, as these modes break the symmetry in field strength between sample and reference positions. This appendix outlines how to undertake the optimization.

A rectangular coaxial line, like any two-conductor line, supports a transverse electromagnetic (TEM) wave at all frequencies. Figure 11(ii) shows its electric and magnetic field configurations. The TEM mode has the desirable property that its magnetic fields lie in a plane perpendicular to the direction of propagation, forming closed loops around the centre conductor. Conservation of magnetic flux then leads to a fixed, frequency-independent relation between the fields on either side of the septum. These fields will also be quite homogeneous, as long as the height  $C$  of the centre conductor is large compared to the gap  $(B - D)/2$  between the centre and outer conductors. To deliver microwave power efficiently to the sample region the characteristic impedance of the TEM mode must be close to that of the cylindrical coaxial line used to bring microwaves into the cryostat. Gunston<sup>24</sup> has tabulated data on the impedance of rectangular coaxial line, and gives some useful approximate formulas. The following expression, due to Bräckelmann, is stated to be

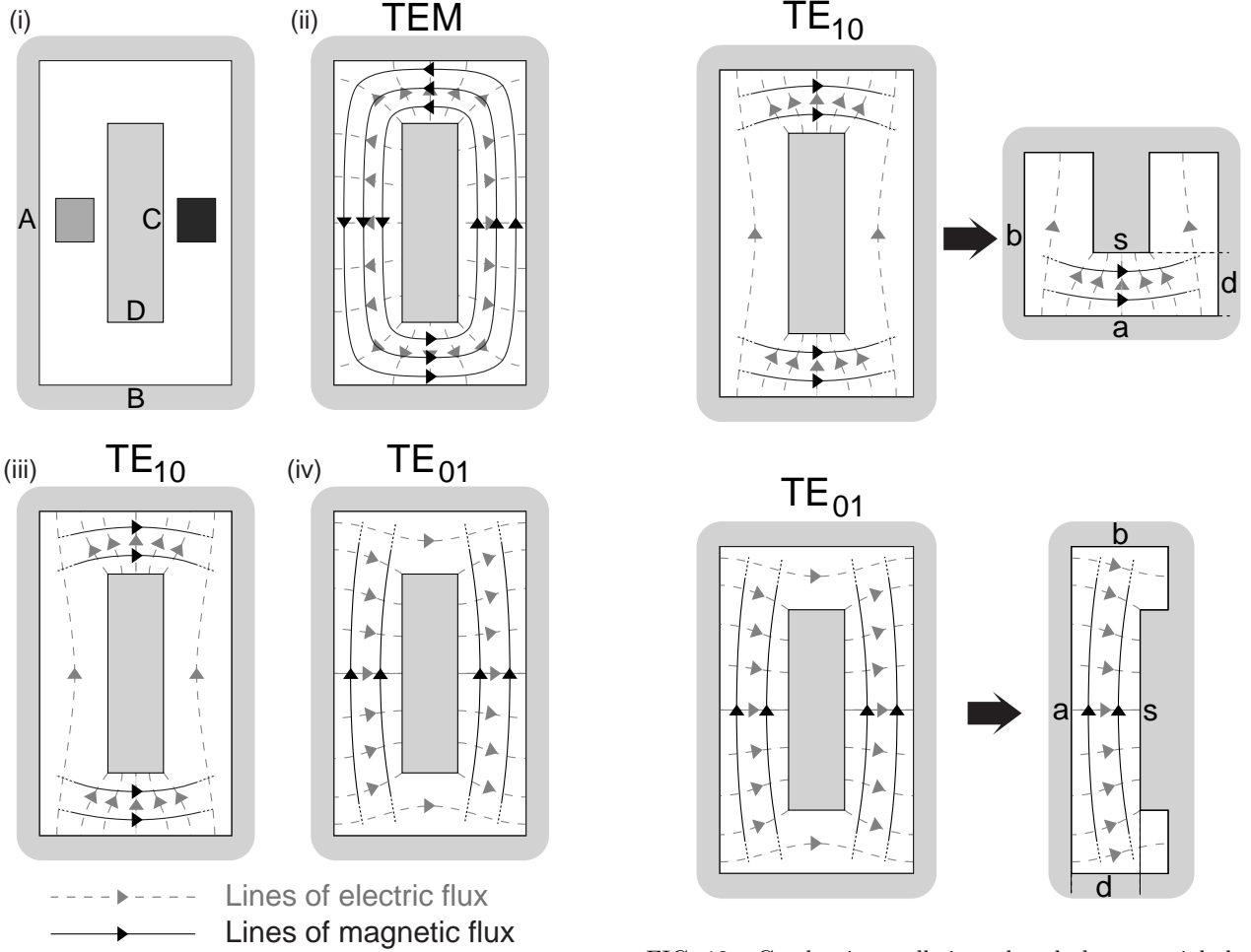


FIG. 11: Cross sections of the rectangular coaxial transmission line: (i) physical layout of the transmission line showing dimensions ( $A, B, C, D$ ) of the inner and outer conductors, and sample and reference positions (shaded squares); (ii) fields of the TEM mode, showing how continuity of flux and a broad, flat inner conductor produce uniform, well polarized fields of equal intensity and opposite direction at the sample and reference positions; (iii) fields of the  $TE_{10}$  mode; and (iv) fields of the  $TE_{01}$  mode. (Magnetic fields of the transverse electric modes contain a component along the direction of propagation and do not form closed loops in the transverse plane.) It is clear that the  $TE_{01}$  mode is most harmful to the operation of the broadband apparatus: its magnetic fields have high intensity at the sample and reference positions and break the balance that otherwise exists in the TEM mode.

accurate to 10% for  $D/B < 0.3$  and  $C/A < 0.8$ :

$$Z_0\sqrt{\epsilon_r} = 59.952 \ln\left(\frac{A+B}{C+D}\right) \Omega, \quad (\text{B1})$$

where  $\epsilon_r$  is the relative permittivity of the dielectric filling the transmission line.

We now come to the question of what places an upper limit on the useful frequency range of the rectangular coaxial waveguide. At high frequencies our method,

FIG. 12: Conducting walls introduced along special electric equipotentials allow the waveguide modes of rectangular coaxial line to be mapped onto the fundamental mode of ridged waveguide, a problem extensively studied in the literature. The figures show the relabelling of dimensions in Pyle's notation<sup>25</sup> as  $a, b, d$  and  $s$ .

which incorporates an in-situ power meter, suffers a spectacular breakdown in the ratio of the relative strengths of the microwave magnetic fields at the sample and reference positions, as shown in Figure 5. This is caused by the presence of higher-order waveguide modes, which have different character from that of the TEM mode under the mid-plane reflection symmetries of the rectangular line. The waveguide modes with the lowest cut-off frequencies are the transverse electric modes  $TE_{10}$  and  $TE_{01}$ , shown in Figures 11(iii) and 11(iv) respectively. These have the property that magnetic fields on opposite sides of the septum point in the *same* direction. The fields of the TEM mode, in contrast, are *antiparallel*, causing an admixture of TEM and TE modes to lack the important characteristic of equal field intensities at sample and reference positions. Particularly damaging is the  $TE_{01}$  mode, which is not screened by the septum and has high field intensity in the vicinity of the sample and reference. In principle it is possible to avoid exciting the

transverse electric modes by building a very symmetric transmission line. In practice, however, we find this to be impossible — sufficiently large symmetry-breaking perturbations are always present. Nevertheless, maintaining high symmetry is still desirable. A comparison of our results with calculations of the cut-off frequencies of the transverse electric modes shows that at frequencies where the higher order modes are free to propagate, they do not immediately cause a breakdown in field ratio: this only occurs when the transverse electric modes come into resonance. (This can be seen very clearly in Figure 5.) As a result, the range of operating frequency can be extended by as much as 50% just by shortening the final section of transmission line and carefully designing the transition between the cylindrical and rectangular sections.

Optimizing the range of single-mode operation of the rectangular transmission line requires a method for calculating the cut-off frequencies of the  $TE_{10}$  and  $TE_{01}$  modes. While waveguide modes in two-conductor rectangular transmission lines have not been extensively studied, their field configurations can be mapped onto a more common geometry: that of ridged waveguide. Figure 12 shows how. Electric equipotentials run perpendicular to lines of electric flux, and special equipotentials, corresponding to local minima of the magnetic flux density, exist on the symmetry axes of the rectangle. A conducting wall can be introduced along these lines without disturbing the field distributions, thereby mapping each mode onto an equivalent ridged waveguide. Figure 12 illustrates the two different ways this is done, for the  $TE_{10}$  and  $TE_{01}$  modes respectively. A very early calculation of the cutoff frequency of ridged waveguide was carried out by Pyle<sup>25</sup> and is notable for its simplicity, generality and enduring accuracy when compared to more recent numerical methods.<sup>26</sup> Pyle's approach is to solve for the transverse resonance condition of the waveguide, which is equivalent to finding the cut-off frequency  $\omega_c$ . We have used this method in our design process, as it is easy to implement (involving only algebraic equations) and is accurate to several percent except when the septum becomes very thin. The length  $\ell$  of the rectangular line, the cut-off frequency, and the discontinuity capacitance of the cylindrical-to-rectangular transition together determine the resonant frequencies  $\omega_R$  of the transverse electric modes. There are two limiting cases, corresponding to open-circuit ( $\ell = \lambda/4$ ) and short-circuit ( $\ell = \lambda/2$ ) termination (where  $\lambda = 2\pi/k$  is the wavelength along the guide), that follow from the waveguide dispersion relation.

$$\omega_R^2 = \omega_c^2 + c^2 k^2 = \omega_c^2 + \frac{4c^2 \pi^2}{\lambda^2} \quad (B2)$$

$$= \omega_c^2 + \frac{c^2 \pi^2}{4\ell^2} : \text{open circuit} \quad (B3)$$

$$= \omega_c^2 + \frac{c^2 \pi^2}{\ell^2} : \text{short circuit} \quad (B4)$$

A high capacitance for the TE modes at the transition from cylindrical to rectangular coax is clearly favourable:

it better approximates the short circuit termination condition and leads to resonant frequencies at the upper end of the range. This effect is responsible for the difference in resonant frequencies between the scale model and the actual apparatus seen in Figure 5. There is, however, a trade-off to be made: too large a transition capacitance for the TEM mode will result in most of the microwave power being reflected before it reaches the sample. The dimensions of the rectangular guide in our apparatus are  $A = 8.90$  mm,  $B = 4.06$  mm,  $C = 4.95$  mm,  $D = 0.91$  mm and  $\ell = 6.60$  mm. The cut-off frequencies for the  $TE_{10}$  and  $TE_{01}$  modes are calculated to be 19.68 GHz and 15.38 GHz respectively. The quarter wave-resonances would then occur at 22.72 GHz and 19.12 GHz, and the half wave resonances at 30.06 GHz and 27.44 GHz.

### APPENDIX C: EXTRACTION OF $\sigma_1(\omega)$ FROM $R_s(\omega)$ MEASUREMENTS

In this appendix we show how the microwave conductivity spectrum of a superconductor can be obtained from a measurement of its frequency-dependent surface resistance. This process is similar to the extraction of conductivity spectra in the infra-red frequency range from reflectance measurements. In both cases, we begin with incomplete information about the electrodynamic response: the bolometric technique described in this paper measures only the *resistive* part of the surface impedance; and optical techniques typically obtain the magnitude, but not the phase, of the reflectance. However, the conductivity  $\sigma \equiv \sigma_1 - i\sigma_2$  is a causal response function, and its real and imaginary parts are related by a Kramers-Krönig transform:

$$\sigma_2(\omega) = \frac{2\omega}{\pi} \mathcal{P} \int_0^\infty \frac{\sigma_1(\Omega)}{\Omega^2 - \omega^2} d\Omega, \quad (C1)$$

where  $\mathcal{P}$  denotes the principle part of the integral. At first sight we seem to have replaced one uncertainty, incomplete knowledge of the phase, by another, the finite frequency range over which the measurements have been made. However, a suitable extrapolation of the data out of the measured frequency range is usually possible and makes the transform a well-defined procedure in practice.

We consider the limit of local electrodynamics, in which the microwave surface impedance  $Z_s$  is related to the complex conductivity in a straightforward manner by the expression

$$Z_s = R_s + iX_s = \sqrt{\frac{i\omega\mu_0}{\sigma_1 - i\sigma_2}}. \quad (C2)$$

Very generally, the conductivity can be partitioned into a superfluid part  $\sigma_S$ , consisting of a zero-frequency delta function and an associated reactive term, and a normal-fluid component  $\sigma_N$ :

$$\sigma(\omega, T) = \sigma_{1S} - i\sigma_{2S} + \sigma_{1N} - i\sigma_{2N} \quad (C3)$$

$$= \pi \frac{n_s e^2}{m^*} \delta(\omega) - i \frac{n_s e^2}{m^* \omega} + \sigma_{1N} - i\sigma_{2N},$$

where  $m^*$  is the quasiparticle effective mass. In the clean-limit, where the quasiparticle scattering rate  $1/\tau$  is much less than the spectroscopic gap  $2\Delta$ , sum-rule arguments enable a clean partitioning of the conduction electron density  $n$  into a superfluid density  $n_s$  and a normal-fluid density  $n_n = n - n_s$ . In this type of generalized two-fluid model,<sup>27</sup> the temperature dependence of  $n_s$  is determined phenomenologically from measurements of the magnetic penetration depth  $\lambda$  through the relation

$$n_s(T)e^2/m^* = [\mu_0\lambda^2(T)]^{-1}. \quad (\text{C4})$$

Applying this, we can write the conductivity at finite frequencies as

$$\sigma(\omega, T) = \sigma_{1N}(\omega, T) - i \left[ \sigma_{2N}(\omega, T) + \frac{1}{\mu_0\omega\lambda^2(T)} \right]. \quad (\text{C5})$$

From Eq. C2 it is clear that  $R_s(\omega)$  is determined by both the real and imaginary parts of the conductivity. However, one simplification occurs at temperatures well below  $T_c$ , where few thermally excited quasiparticles exist, and the low frequency reactive response is dominated by the superfluid. In this case, a good approximation to the relations becomes

$$\begin{aligned} R_s(\omega, T) &= \frac{1}{2}\mu_0^2\omega^2\lambda^3(T)\sigma_1(\omega, T), \\ X_s(\omega, T) &= \mu_0\omega\lambda(T). \end{aligned} \quad (\text{C6})$$

At higher frequencies and temperatures, a more complete treatment would account for quasiparticle contributions to field screening, which enter through  $\sigma_{2N}(\omega, T)$ . We use an iterative procedure to obtain the quasiparticle conductivity spectrum  $\sigma_{1N}(\omega)$ , starting from the good initial guess provided by Eq. C6. The process goes as follows. A phenomenological form that captures the key characteristics of the dataset but has no physical motivation, namely  $\sigma_1(\omega) = \sigma_0/[1 + (\omega/\Gamma)^y]$ , is fitted to the spectrum and used to extrapolate out of the measured frequency range. The Kramers–Krönig transform (Eq. C1) can then be applied to obtain  $\sigma_{2N}(\omega)$ . With  $\sigma_{2N}(\omega)$  in

hand, and with the superfluid contribution to  $\sigma_2$  known from measurements of the magnetic penetration depth, a new extraction of the conductivity from the  $R_s(\omega)$  data is made, this time using the *exact* expression, Eq. C2. The whole procedure is repeated to self-consistency. We find that the procedure is stable and converges rapidly, and is not sensitive to the details of the high-frequency extrapolation. Also, the corrections are quite small for the low temperature dataset shown in Fig. 8: at the highest temperature and frequency they amount to a 7% change in  $\sigma_1$ .

In addition, two independent experimental checks give us further assurance that we obtain the correct conductivity spectra. We first note that Eq. C2 contains an expression for the surface reactance  $X_s$ . Therefore, once we have measured the penetration depth and extracted the conductivity spectra from the  $R_s(\omega)$  data, we can predict the temperature dependence of the surface reactance at *any* frequency and compare with experiment. We have made this comparison at 22.7 GHz, with surface reactance data obtained on the same crystal, and find excellent agreement. We note that this is a frequency high enough for quasiparticle scattering to have a discernible effect on the surface reactance.

A second verification of the conductivity extraction procedure is its ability to predict the spectral weight that resides *outside* the frequency window of the measurement. A corollary of the Kramers–Krönig relation C1 is the oscillator-strength sum rule

$$\frac{ne^2}{m^*} = \frac{2}{\pi} \int_0^\infty \sigma_1(\omega, T) d\omega. \quad (\text{C7})$$

In a superconductor, in the clean limit, the sum rule requires that any spectral weight disappearing from the superfluid density  $n_s(T)$  as temperature is raised must reappear as an increase in the frequency-integrated quasiparticle conductivity. We have carried out this comparison, which is shown in the inset of Fig. 8.<sup>21</sup> The good agreement in the temperature dependence of the superfluid and normal-fluid densities is a strong verification of both the analysis procedure *and* the bolometric technique.

\* Permanent address: Dept. of Physics, Simon Fraser University, Burnaby, BC, Canada, V5A 1S6.

† Permanent address: Dept. of Physics and Astronomy, McMaster University, Hamilton, ON, Canada, L8S 4M1.

<sup>1</sup> D. A. Bonn, P. Dosanjh, R. Liang and, W. N. Hardy, Phys. Rev. Lett. **68**, 2390 (1992).

<sup>2</sup> D.A. Bonn and W.N. Hardy, in *Physical Properties of High Temperature Superconductors, Vol. V*, ed. D.M. Ginsberg (World Scientific, Singapore, 1996).

<sup>3</sup> R. J. Ormeno, D. C. Morgan, D. M. Broun, S. F. Lee, and, J. R. Waldram, Rev. Sci. Instrum. **68**, 2121 (1997).

<sup>4</sup> A. Hosseini et al., Phys. Rev. B **60**, 1349 (1999).

<sup>5</sup> P. J. Hirschfeld and W. A. Atkinson, J. Low Temp. Phys. **127**, 289 (2002).

<sup>6</sup> M. H. Hettler and P. J. Hirschfeld, Phys. Rev. B **61**, 11313 (2000).

<sup>7</sup> A. J. Berlinsky, D. A. Bonn, R. Harris, and C. Callin, Phys. Rev. B **61**, 9088 (2000).

<sup>8</sup> M. A. Biondi and M. P. Garfunkel, Phys. Rev. **116**, 853 (1959).

<sup>9</sup> Y. Matsuda et al., Phys. Rev. B **49**, 4380 (1994); O. K. C. Tsui et al., Phys. Rev. Lett. **73**, 724 (1994); M. Gaifullin et al., Phys. Rev. Lett. **83**, 3928 (1999).

<sup>10</sup> A. Hosseini, Saeid Kamal, D. A. Bonn, Ruixing Liang, and

- W. N. Hardy, Phys. Rev. Lett. **81**, 1298 (1998).
- <sup>11</sup> In general, the thermal model of the bolometer stage should include a distributed heat capacity through which the thermal currents flow. However, we show in Appendix A that a necessary condition for optimal sensitivity is that the thermal weak link be operated in the low frequency limit where it *is* well approximated by a lumped thermal mass and a weak thermal link having negligible heat capacity.
- <sup>12</sup> J. M. Gildemeister, A. T. Lee, and P. L. Richards, Appl. Phys. Lett. **74**, 868 (1999).
- <sup>13</sup> S. Sridar and W. L. Kennedy, Rev. Sci. Instrum. **59**, 531 (1988). D. L. Rubin et al., Phys. Rev. B **38**, 6538 (1988).
- <sup>14</sup> Cernox™ resistor, model CX-1050-BC, was purchased from Lake Shore Cryotronics, Inc. of 575 McCorkle Boulevard, Westerville, Ohio 43082 USA.
- <sup>15</sup> Dow Corning #976V High Vacuum Grease, Dow Corning Corporation P.O. Box 0994 Midland, Michigan 48686-0994 USA.
- <sup>16</sup> 1.50 k $\Omega$  thin-film surface-mount resistors, model SOTA # S0303AS1501FKW, were purchased from State of the Art, Inc. of 2470 Fox Hill Rd., State College, Pennsylvania 16803-1797 USA.
- <sup>17</sup> Stycast 2850FT, Emerson and Cumming Inc., Canton, Massachusetts 02021 USA.
- <sup>18</sup> We use standard 50  $\Omega$  impedance semi-rigid coaxial line having a Teflon dielectric and a 0.141" diameter outer conductor made from stainless steel and 0.0359" diameter inner conductor made from silver-plated, copper-clad steel.
- <sup>19</sup> R. P. Elliott and F. A. Shunk, Bull. Alloy Phase Diagrams **1**, 2, 45 (1980).
- <sup>20</sup> A. A. Abrikosov, Fundamentals of the Theory of Metals (North-Holland, New York, 1988).
- <sup>21</sup> P. J. Turner, R. Harris, Saeid Kamal, M. E. Hayden, D. M. Broun, D. C. Morgan, A. Hosseini, P. Dosanjh, G. K. Mullins, J. S. Preston, Ruixing Liang, D. A. Bonn, and W. N. Hardy, et al., Phys. Rev. Lett. **90**, 237005 (2003).
- <sup>22</sup> J. Corson, J. Orenstein, Seongshik Oh, J. O'Donnell, and J. N. Eckstein, Phys. Rev. Lett. **85**, 2569 (2000).
- <sup>23</sup> A. Janossy, A. Rockenbauer, and S. Pekker, Physica **C167**, 301 (1990); A. Janossy, L.-C. Brunel, and J. R. Cooper, Phys. Rev. B **54**, 10186 (1996).
- <sup>24</sup> M. A. R. Gunston, *Microwave Transmission-Line Impedance Data* (Van Nostrand Reinhold, London, 1971).
- <sup>25</sup> J. R. Pyle, IEEE. Trans. Microwave Theory Tech. **MTT-14**, 175 (1966).
- <sup>26</sup> S. Amari, J. Bornemann, and R. Vahldieck, IEEE. Trans. Microwave Theory Tech. **MTT-44**, 2256 (1996).
- <sup>27</sup> A. J. Berlinsky, C. Kallin, G. Rose, and A. C. Shi, Phys. Rev. B **48**, 4074 (1993).
- <sup>28</sup> D. A. Bonn, Ruixing Liang, T. M. Riseman, D. J. Baar, D. C. Morgan, K. Zhang, P. Dosanjh, T. L. Duty, A. MacFarlane, G. D. Morris, J. H. Brewer, W. N. Hardy, C. Callin, and A. J. Berlinsky, Phys. Rev. B **47**, 11314 (1993).